Mercury's magnetopause and bow shock from MESSENGER Magnetometer observations

Reka M. Winslow,[1] Brian J. Anderson,[2] Catherine L. Johnson,[1,3] James A. Slavin,[4] Haje Korth,[2] Michael E. Purucker,[5] Daniel N. Baker,[6] and Sean C. Solomon[7,8]

Received 21 June 2012; revised 13 March 2013; accepted 15 March 2013; published 28 May 2013.

[1] We have established the average shape and location of Mercury's magnetopause and bow shock from orbital observations by the MESSENGER Magnetometer. We fit empirical models to midpoints of boundary crossings and probability density maps of the magnetopause and bow shock positions. The magnetopause was fit by a surface for which the position **R** from the planetary dipole varies as $[1+\cos(\theta)]^{-\alpha}$, where θ is the angle between **R** and the dipole-Sun line, the subsolar standoff distance R_{ss} is 1.45 R_M (where R_M is Mercury's radius), and the flaring parameter $\alpha = 0.5$. The average magnetopause shape and location were determined under a mean solar wind ram pressure P_{Ram} of 14.3 nPa. The best fit bow shock shape established under an average Alfvén Mach number (M_A) of 6.6 is described by a hyperboloid having $R_{ss} = 1.96\ R_M$ and an eccentricity of 1.02. These boundaries move as P_{Ram} and M_A vary, but their shapes remain unchanged. The magnetopause R_{ss} varies from 1.55 to 1.35 R_M for P_{Ram} in the range of 8.8–21.6 nPa. The bow shock R_{ss} varies from 2.29 to 1.89 R_M for M_A in the range of 4.12–11.8. The boundaries are well approximated by figures of revolution. Additional quantifiable effects of the interplanetary magnetic field are masked by the large dynamic variability of these boundaries. The magnetotail surface is nearly cylindrical, with a radius of ~2.7 R_M at a distance of 3 R_M downstream of Mercury. By comparison, Earth's magnetotail flaring continues until a downstream distance of ~10 R_{ss}.

Citation: Winslow, R. M., B. J. Anderson, C. L. Johnson, J. A. Slavin, H. Korth, M. E. Purucker, D. N. Baker, and S. C. Solomon (2013), Mercury's magnetopause and bow shock from MESSENGER Magnetometer observations, *J. Geophys. Res. Space Physics*, *118*, 2213–2227, doi:10.1002/jgra.50237.

1. Introduction

[2] The boundaries of Mercury's magnetosphere reflect fundamental processes of the solar wind interaction with the planet's dipolar magnetic field [*Russell et al.*, 1988; *Slavin*, 2004]. These boundaries are the bow shock, across which the solar wind is compressed and deflected around Mercury, and the magnetopause, which is the current layer separating the shocked solar wind plasma and interplanetary magnetic field (IMF) from the planetary magnetic field. The bow shock is a fast magnetosonic shock wave that "stands" in the solar wind while diverting the solar wind around the planet's magnetospheric cavity [*Spreiter et al.*, 1966]. The bow shock changes shape and stands closer or farther from the planet in response to variations in solar wind Mach number and, to a lesser extent, IMF direction [*Spreiter et al.*, 1966; *Slavin and Holzer*, 1981; *Peredo et al.*, 1995]. The magnetopause location and shape are determined principally by the pressure exerted on the magnetopause by the shocked solar wind plasma, which scales with the solar wind ram pressure, balanced by the planetary magnetic field [*Spreiter et al.*, 1966; *Farris and Russell*, 1994]. Accordingly, the dynamic pressure of the solar wind and the magnetic pressure of the magnetosphere are the dominant factors determining the location and shape of the magnetopause.

[3] Because the distribution of magnetic flux within a magnetosphere is determined both by the intrinsic planetary field and the external currents, magnetic reconnection, which drives some of these external currents, also affects magnetopause shape and position. Most important among these reconnection-driven effects are the inward "erosion" of the dayside magnetopause to lower altitudes by transfer of magnetic flux to the tail [*Holzer and Slavin*, 1978] and the outward "flaring" of the nightside magnetopause as the

Additional supporting information may be found in the online version of this article.

[1]Department of Earth, Ocean and Atmospheric Sciences, University of British Columbia, Vancouver, British Columbia, Canada.
[2]The Johns Hopkins University Applied Physics Laboratory, Laurel, Maryland, USA.
[3]Planetary Science Institute, Tucson, Arizona, USA.
[4]Department of Atmospheric, Oceanic and Space Sciences, University of Michigan, Ann Arbor, Michigan, USA.
[5]NASA Goddard Space Flight Center, Greenbelt, Maryland, USA.
[6]Laboratory for Atmospheric and Space Physics, University of Colorado, Boulder, Colorado, USA.
[7]Department of Terrestrial Magnetism, Carnegie Institution of Washington, Washington, D. C., USA.
[8]Lamont-Doherty Earth Observatory, Columbia University, Palisades, New York, USA.

Corresponding author: R. M. Winslow, Department of Earth, Ocean and Atmospheric Sciences, University of British Columbia, Vancouver, BC, V6T 1Z1, Canada. (rwinslow@eos.ubc.ca)

2169-9380/13/10.1002/jgra.50237

magnetotail is loaded with magnetic flux [*Caan et al*., 1973]. These expansions and contractions of the dayside and nightside magnetosphere take place on time scales comparable to the Dungey cycle that governs the circulation of magnetic flux and plasma within the magnetospheres of Earth-like planets. The characteristic time scale of the Dungey cycle is ~1 h at Earth and ~2 min at Mercury [*Slavin et al*., 2009].

[4] It has been suggested that reconnection may have a greater effect on magnetopause location at Mercury than at Earth [*Slavin and Holzer*, 1979]. This prediction has been supported by the extreme loading and unloading of Mercury's magnetotail observed during the third flyby of Mercury by the MErcury Surface, Space ENvironment, GEochemistry, and Ranging (MESSENGER) spacecraft [*Slavin et al*., 2010, 2012a]. Further, it has also been predicted that magnetic fields associated with induction currents in Mercury's interior may act to oppose and limit the solar wind's ability to compress or expand the extent of the dayside magnetosphere [*Seuss and Goldstein*, 1979; *Goldstein et al*., 1981; *Grosser et al*., 2004; *Glassmeier et al*., 2007]. Mercury has an internally generated, axially aligned dipolar magnetic field with a moment of 190–195 nT R_M^3 (where R_M is Mercury's mean radius, 2440 km) that is offset northward from the geographic equator by 0.2 R_M [*Anderson et al*., 2011, 2012; *Johnson et al*., 2012]. The combination of a weak dipole moment, the absence of a conducting ionosphere (i.e., no magnetosphere-ionosphere coupling), and the predominantly quasiparallel subsolar shock conditions (due to the small Parker spiral angle at Mercury's orbit) distinguish Mercury from other planets in our solar system that possess magnetic fields.

[5] The Earth's bow shock has been studied extensively both observationally and theoretically [e.g., *Peredo et al*., 1995]. It is a highly dynamic boundary, controlled by temporal variations in solar wind characteristics. The general shape of the shock has been investigated with empirical models [e.g., *Fairfield*, 1971; *Slavin and Holzer*, 1981], gas dynamic flow models [e.g., *Slavin et al*., 1983a; *Verigin et al*., 2003a], and magnetohydrodynamic models [e.g., *Chapman and Cairns*, 2003] and is well described by a conic section. *Formisano et al*. [1971] found that the subsolar bow shock position moves outward during conditions of low Alfvén Mach number (M_A). *Peredo et al*. [1995] confirmed that M_A primarily controls the bow shock shape, but in contrast to the findings of the earlier study [*Formisano et al*., 1971], they observed that the subsolar shock moves earthward and the flanks flare outward during times of low M_A.

[6] The average shape of the terrestrial magnetopause has been described with several empirical models [e.g., *Shue et al*., 1997; *Boardsen et al*., 2000; *Lin et al*., 2010] and magnetohydrodynamic models [*Lu et al*., 2011]. The dynamic pressure of the solar wind affects the size of the magnetospheric cavity as well as the shape of the magnetopause. The subsolar magnetopause standoff distance is observed to decrease with increased dynamic pressure [*Sibeck et al*., 1991; *Fairfield*, 1995], and the boundary shape is observed to flare with increased pressure [*Shue et al*., 1997]. Reconnection-related effects can also influence the dayside magnetopause location and the flaring of the tail. On the dayside, a southward IMF component will facilitate reconnection at low latitudes, which can erode the magnetopause near the subsolar point and flare the magnetopause on the nightside by adding flux to the tail. The magnetopause has been observed to move planetward by as much as 1–2 R_E (where R_E is Earth's radius) due to the erosion of the boundary under southward IMF [*Coroniti and Kennel*, 1972; *Holzer and Slavin*, 1978; *Sibeck et al*., 1991]. However, a statistical study of these effects at Mercury with a large database of magnetopause crossings, such as the one reported here, would require knowledge of IMF direction on time scales of 1 min or less because of the very short Dungey cycle time at Mercury. The lack of an upstream monitor therefore limits the scope of our investigation with respect to the effects of reconnection on magnetopause position.

[7] The solar wind and IMF play major roles in influencing the bow shock and magnetopause, and those roles must be understood quantitatively in order to model the internal magnetic field, the magnetosphere–solar wind interaction, and the access of solar wind and magnetospheric charged particles to the planetary surface. At Mercury the solar wind density is approximately an order of magnitude higher and the IMF magnitude a factor of ~5 higher than at Earth [*Korth et al*., 2010], whereas the planetary magnetic moment is only 0.06% of Earth's. Mercury's orbit is eccentric, so the planet is subjected to different solar wind conditions at perihelion and aphelion. Mercury's magnetopause and bow shock have been studied from limited data obtained during flybys by the Mariner 10 [*Russell*, 1977] and MESSENGER spacecraft [*Slavin et al*., 2009]. *Russell* [1977] fit shape models to both the magnetopause and bow shock with data from the two Mariner 10 flybys, and *Slavin et al*. [2009] updated these boundary shapes with MESSENGER flyby data. *Slavin et al*. [2009] also looked at the boundary crossings during northward IMF from data taken during the first MESSENGER flyby. However, even the combined Mariner 10 and MESSENGER flyby data set comprised only six pairs of bow shock and magnetopause crossing points.

[8] In this paper, we present analyses of Mercury's bow shock and magnetopause shape obtained from orbital magnetic field observations by the MESSENGER spacecraft over a span of 3 Mercury years under a variety of IMF and solar wind conditions. The objective of this study is to characterize the underlying shapes of both the magnetopause and bow shock and, insofar as the data permit, to assess how these shapes are affected by the solar wind and IMF. We have analyzed the observations in two ways. First, from the locations of the inner and outer magnetopause and bow shock crossings, we defined a mean crossing point and we found the average boundary shape from the ensemble of crossing points. In the second method, the probability of spacecraft residence within the range of magnetopause or bow shock crossings on each pass has been used to build a probability density map of the two boundaries. In section 2, we describe the magnetic field observations and how the boundaries were identified. In section 3, we establish the general shape of both the magnetopause and the bow shock from the mean locations (section 3.1) and the probability densities (section 3.2). In section 4, we assess how the boundaries respond to solar wind forcing, and the results and conclusions are given in sections 5 and 6, respectively.

2. Magnetic Field Observations: Boundary Identifications

[9] The MESSENGER spacecraft was inserted into orbit about Mercury on 18 March 2011. The initial orbit had a 200 km periapsis altitude, 82.5° inclination, 15,300 km apoapsis altitude, and 12 h period. During each orbit, MESSENGER typically spent 1–2 h inside the magnetosphere; the rest of the time was spent in the magnetosheath and in the interplanetary medium. For this study, we used 3 Mercury years of MESSENGER Magnetometer (MAG) [*Anderson et al*., 2007] data starting on 23 March 2011 and extending through 19 December 2011, providing repeated coverage at all local times. To conserve data volume during this period, MAG operated at variable sample rates, with high-rate (20 samples/s) data collection primarily in effect during transits of the magnetosphere. Sample rates in the interplanetary medium were at least as high as 2 samples/s or higher and a channel to record fluctuations at 1–10 Hz operated continuously to provide an uninterrupted measure of the field variability.

[10] Magnetic field data were analyzed in Mercury solar orbital (MSO) coordinates. In MSO coordinates, X_{MSO} is positive sunward, Z_{MSO} is positive northward, Y_{MSO} is positive duskward and completes the right-handed system, and the origin is at the center of the planet. To analyze boundary locations the spacecraft positions were translated into a system centered on the planetary dipole [*Anderson et al*., 2012]. The vector components of the magnetic field in the planet-centered and dipole-centered systems are identical. Because the bow shock and magnetopause are ordered by the solar wind flow in the frame of Mercury's orbital motion, the spacecraft position data were transformed into an aberrated system such that the $+X$ direction is antiparallel to the solar wind velocity relative to Mercury. The average aberration angle at Mercury is about 7° toward dawn. However, because of Mercury's variation in orbital speed between perihelion and aphelion, as well as variability in the solar wind speed, the aberration angle varied by a factor of about 3, from 3.5° to 10.2°, during the period of our study. The aberration correction for both the magnetopause and the bow shock crossings was calculated from the planet's instantaneous orbital speed together with predictions of solar wind speed obtained from the ENLIL heliospheric model [*Odstrcil*, 2003] within 4 min of the times of the boundary crossings. Because the Fast Imaging Plasma Spectrometer (FIPS) on MESSENGER does not typically see the solar wind, we do not have in situ estimates of solar wind properties, so we use ENLIL model predictions of solar wind parameters in this study. Use of model predictions for the solar wind parameters introduces some level of uncertainty into the normalized boundary shapes derived in section 4 of the paper, with the highest uncertainty most likely introduced for the cases of extreme events, when the solar wind pressure is predicted to be highest. Benchmarking of the ENLIL model at Mercury has been initiated [*Gershman et al*., 2012; *Baker et al*., 2013]; however, the long-time-scale (>44 day) variations in the model outputs that are modulated by Mercury's orbital distances from the Sun are persistent over the 3 Mercury years of data analyzed here. Our aim here is not to use ENLIL for event studies but to capture the average annual variation in the solar wind ram pressure and density and use these variations to correct our average boundary shapes.

[11] The IMF magnitude assigned to each crossing was evaluated as a 1 h average of MAG data upstream of the outermost bow shock encounter. The Alfvén Mach number $M_A = \frac{v_{sw}}{[B_{IMF}/(\mu_0\rho)^{0.5}]}$, where v_{sw} is the solar wind speed, B_{IMF} is the magnetic field magnitude in the IMF, μ_0 is the magnetic permeability of free space, and ρ is the solar wind plasma density, was calculated using IMF values that were estimated from the 1 h IMF averages and ENLIL model-generated solar wind speed and density. We have shown previously that the 1 h IMF averages are suitable for determining the IMF B_X direction, which is the dominant IMF component at Mercury, but they are not suitable for establishing the IMF B_Y and B_Z directions, which vary on time scales less than 1 h [*Winslow et al*., 2012]. The magnitude of the IMF is dominated by the B_X component and is thus also steady on the 1 h time scale, i.e., the average duration of a transit of the magnetosphere by the MESSENGER spacecraft. The resolution of these measurements is suitable for investigating the effect of solar wind pressure and Alfvén Mach number on magnetopause and bow shock positions, but not the reconnection-driven effects that depend on IMF orientation and take place on time scales of 1 min to a few minutes [*Slavin et al*., 2009, 2010].

[12] Magnetopause and bow shock crossings were identified on every orbit, both before and after the magnetospheric transit and denoted as the inbound and outbound crossings, respectively. On almost every orbit, multiple crossings of each boundary were observed as a result of motion of the boundary relative to the spacecraft. Although the repeated crossings were often difficult to distinguish individually, the first and last boundary encounters were readily identified. Thus, rather than attempt uncertain identifications of every boundary crossing within each passage through the boundary region, we identified the times of the innermost and outermost crossing on each pass for the bow shock and magnetopause. Our approach has the added benefit that each pass corresponds to an independent sample of external IMF and solar wind conditions, whereas statistical analyses that count every crossing equally in passes with multiple crossings will overweight such passes. We aim to provide demarcations for the inner and outer limits of the boundaries, within and outside of which the spacecraft was clearly located in the magnetosphere, magnetosheath, or interplanetary medium. Wave characteristics (including foreshock waves, nonlinear quasiparallel shock phenomena, and magnetopause boundary waves) are beyond the scope of this paper.

[13] All boundary crossings were picked by visual inspection with the following criteria. For the bow shock, the inbound outer limit was identified as the time at which the first sharp increase in the magnitude $|\mathbf{B}|$ of the magnetic field was observed. The inner limit was identified as the time of the last sharp increase in $|\mathbf{B}|$. These criteria worked well when the IMF was oriented somewhat oblique to the planet-Sun line, that is, for quasi-perpendicular shock conditions. A perpendicular shock forms when the shock-normal direction is perpendicular to the IMF direction, whereas a parallel shock occurs when the shock normal is parallel or antiparallel to the IMF. For near-parallel shock conditions,

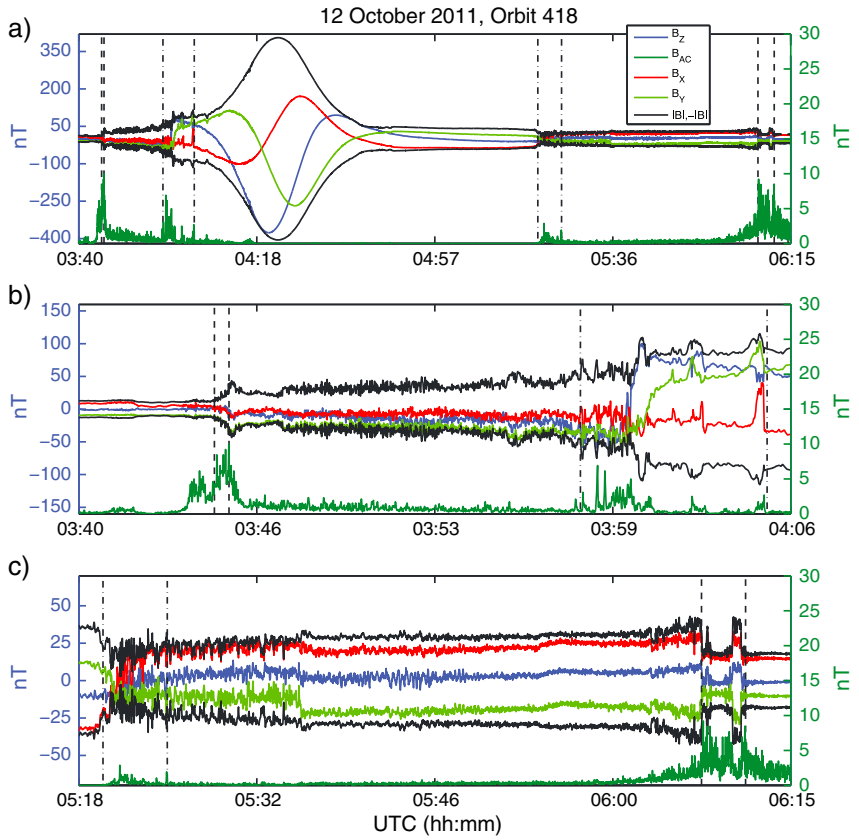

Figure 1. (a) MESSENGER Magnetometer data for the first magnetospheric transit on 12 October 2011 (orbit 418). Left axes give the scales for B_X (red), B_Y (light green), B_Z (blue), and |**B**| and −|**B**| (black); the right axis is the scale for B_{AC} (dark green). Vertical lines denote the crossing times of the inner and outer edges of the bow shock (dashed) and magnetopause (dot-dashed). (b) Close-up view of the inbound portion of the orbit. (c) Close-up view of the outbound portion of the orbit.

there was often little or no increase in |**B**|, but the bow shock boundary was marked by the onset of large variability in |**B**|. Sometimes these modulations grew gradually, in which case we chose the outermost excursions in |**B**| that were distinctly larger than the upstream variability. The outbound bow shock was picked in a similar fashion, that is, a sharp decrease in the field magnitude marked the boundary.

[14] For the magnetopause, the crossings were most readily identified when the shear angle between the direction of the magnetic field in the magnetosphere and that in the magnetosheath was larger than about 45°, because the field rotation is a direct signature of the magnetopause current layer. On the dayside and on the flanks, the shear is typically in B_Y and B_Z, whereas on the nightside the shear is mostly in B_X. The inner boundary was identified by the innermost substantial rotation away from the magnetospheric field direction and the outer boundary by the outermost rotation toward the ambient magnetospheric field direction, excluding the background magnetosheath variability. In many cases, however, the field direction in the magnetosheath was the same as (or close to) that inside the magnetosphere. For example, the magnetic shear can be low at low dayside latitudes when the IMF is northward and on the nightside when the IMF is antisunward such that the southern lobe field is parallel to the draped magnetosheath field. In such cases, although the local magnetic shear is low, there were other signatures in the magnetic field that indicated transitions between magnetosheath and magnetosphere regimes. These signatures include an increase in magnetic fluctuations in the magnetopause layer (documented from Earth's magnetopause) [*Fuselier et al.*, 1995, 1997] and a change in the character of the low-frequency fluctuations on the magnetosheath side of the boundary. The higher-frequency magnetic fluctuations are recorded by the 1–10 Hz fluctuation channel (or B_{AC}), which provides an average amplitude of the 1–10 Hz band-pass-filtered field. In addition, on the dayside the inner magnetopause boundary is also often indicated by either a stepwise increase in |**B**| or the onset of an inward gradient in |**B**| on the magnetosphere side of the boundary. However, these signatures were not always sharp, and in some cases it was difficult to identify the magnetopause boundary. Boundary crossing choices were made conservatively such that the inner edge was definitely inside the magnetosphere and the outer edge was definitely in the magnetosheath. Using plasma measurements from FIPS to identify the boundary crossings is beyond the scope of this paper and would require careful accounting of the FIPS look direction, since its field of view is ~1.4π sr. Several dozen comparisons show excellent correspondence between the boundaries identified from MAG observations and abrupt changes in FIPS proton count rates.

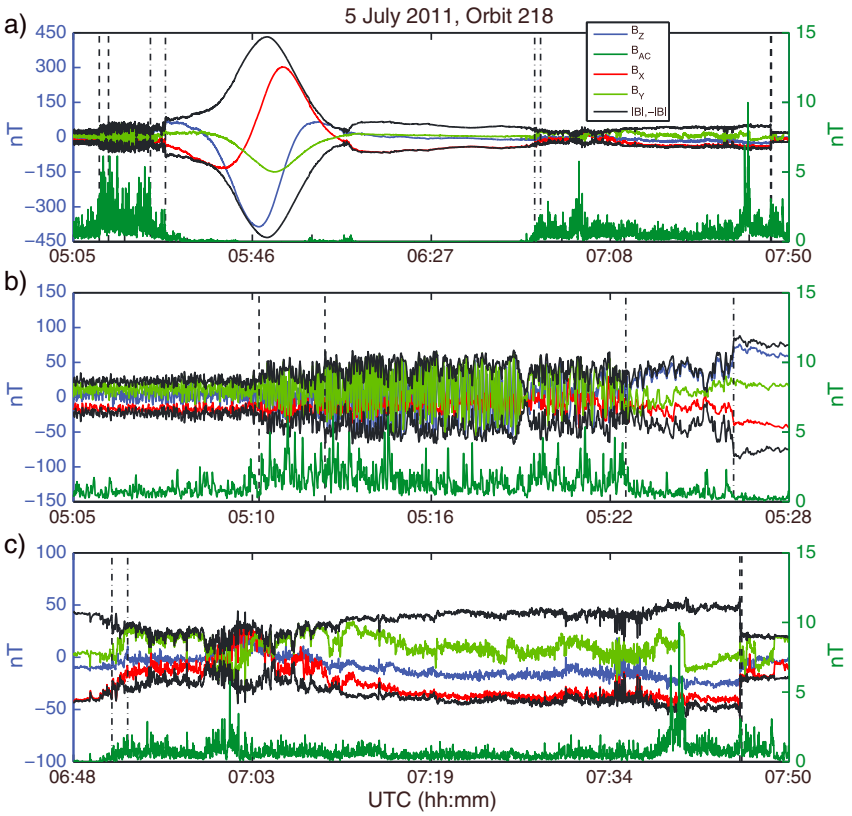

Figure 2. (a-c) MESSENGER Magnetometer data for the first magnetospheric transit on 5 July 2011, orbit 218, in the same format as in Figure 1.

[15] Data from the first magnetospheric transit on 12 October 2011 (orbit 418) are shown in Figure 1 together with expanded views of the inbound and outbound boundary passages. In this case, the shock conditions were oblique (perpendicular shock geometry), and there was high magnetic shear across the magnetopause on both the inbound and outbound crossings. The spacecraft entered the magnetosphere from the dayside and exited on the nightside. The spacecraft first grazed the shock at 3:43:59 Coordinated Universal Time (UTC) before passing through it at 3:45:29 UTC. On this transit, the shock was also marked by an increase in high-frequency fluctuations, B_{AC}, although most of the fluctuations before the shock crossing are attributed to foreshock waves. The spacecraft then traveled through the magnetosheath and encountered the high-shear magnetopause on the dawn side, marked by a rotation in B_Z and B_Y and an increase in B_{AC} shortly before the magnetopause boundary. On the outbound portion of the orbit, the spacecraft first encountered the magnetopause at 5:19:56 UTC and was finally in the magnetosheath at 5:25:05 UTC. The rotation in the magnetic field is evident in B_X as the spacecraft exited the magnetosphere from the southern tail lobe and was also associated with a rise in B_{AC}. The spacecraft then crossed the bow shock twice on its path back into the interplanetary medium.

[16] Often the boundaries were less clear, and Figure 2 shows data from the first magnetospheric transit on 5 July 2011 (orbit 218) with such crossings. On this orbit, the shock was quasiparallel on the dayside, which caused the large modulations in |**B**| near the bow shock crossing. The magnetic field inside the magnetosheath was highly variable, with large, quasiperiodic rotations in B_Y and B_Z up to the magnetopause. The magnetic shear across the magnetopause was low, so the decrease in B_{AC} and the increase in the total field magnitude were taken to indicate the magnetopause crossing. On the outbound part of the orbit, the magnetic shear was again low across the magnetopause, with slight rotations visible in B_Y and B_X, but the crossing was indicated by an increase in B_{AC}. The field magnitude decreased as the spacecraft crossed the magnetopause but increased inside the magnetosheath until it reached the oblique bow shock boundary and decreased abruptly at 7:45:54 UTC.

[17] The times of the inner and outer edges of the recorded magnetopause and bow shock crossings for all the data presented in this study are given in Table S1 in the supporting information. There are 1065 magnetopause and 1084 bow shock crossings altogether in our data set. The number of bow shock crossings exceeds the number of magnetopause crossings because the Magnetometer was switched off to conserve power for parts of 19 orbits during MESSENGER's first long-eclipse season in orbit around Mercury. On these orbits, both the inbound and outbound bow shock crossings were recorded, but typically only the inbound (and not the outbound) magnetopause crossings were observed.

3. Average Boundary Shapes

[18] The first step in analyzing the crossing data was to determine the best boundary shapes for all crossings together,

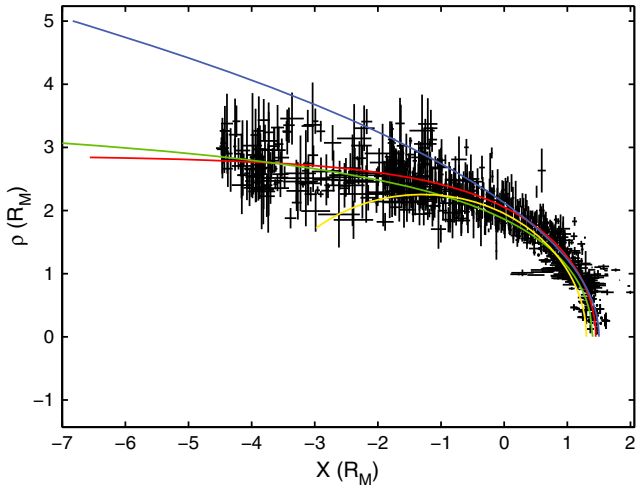

Figure 3. Midpoints between the inner and outer magnetopause crossing positions identified from MESSENGER Magnetometer data from 23 March 2011 through 19 December 2011. Error bars show the distance between the inner and outer crossing. Curves show the best-fit paraboloid (blue) to the dayside crossings and the best-fit Shue et al. model (red), as well as models from previous studies by *Slavin et al.* [2009] (green) and *Russell* [1977] (yellow). The paraboloid has parameters given by $R_{ss} = 1.5\ R_M$ and $\gamma = 1$, whereas the Shue et al. model is given by $R_{ss} = 1.45\ R_M$ and $\alpha = 0.5$.

effectively averaging over IMF and solar wind conditions. This averaging was accomplished by fitting empirical models to the magnetopause and bow shock crossing locations. The boundary locations were specified with two different techniques. First, we used the mean locations of the boundaries and fit empirical shapes to these directly. Second, we used a probabilistic measure of residence within the boundary regions to identify the locations of maximum residence probability. Empirical shapes were then fit to these probability density maps, with the established probabilities used as weights in the fitting. In the analysis that follows, all positions are in aberrated coordinates (X, Y, Z), where X and Y are the aberrated X_{MSO} and Y_{MSO} coordinates, respectively, and $Z = Z_{MSO}$. In addition, we have assumed that the boundaries are figures of revolution about the line through the dipole center that parallels the X axis; the validity of this assumption is quantitatively tested and confirmed in section 5. The northward offset of the planetary dipole is included in the definition of the distance from the axis of revolution, given by $\rho = \sqrt{Y^2 + (Z - Z_d)^2}$, where $Z_d = 0.196\ R_M$ [*Anderson et al.*, 2011, 2012; *Johnson et al.*, 2012].

3.1. Midpoint Fits

[19] In the first approach to determining boundary locations, model curves were fit to the average crossing points, that is, the midpoint between the inner and outer edge of the boundary location on each pass. The inner and outer limits of the boundaries were assigned as the uncertainty range. This method allows direct comparison of our results with approaches that have been used historically to determine boundary shapes [e.g., *Shue et al.*, 1997, *Slavin et al.*, 2009].

3.1.1. Magnetopause

[20] For the magnetopause, we used a paraboloid conic section [*Belenkaya et al.*, 2005; *Alexeev et al.*, 2010] as well as the model shape proposed by *Shue et al.* [1997] to fit our crossings. Figure 3 shows the midpoints of the magnetopause crossings from the 3 Mercury years of data analyzed in this study. To establish a time-averaged magnetopause shape from the crossing points, we modeled them in ρ-X space. In our boundary fits, we used a grid search method that minimized the root mean square (RMS) residual of the perpendicular distance of the observed midpoints from the model boundary.

[21] The paraboloid fit is motivated by the magnetospheric model of *Alexeev et al.* [2010], which was derived with a parabolic parameterization of magnetopause shape. Past studies of the magnetopause shapes around other planets have also involved fits to conic sections [e.g., *Russell*, 1977]. The paraboloid model shape is described by

$$X(\rho) = -\left(\frac{\gamma^2 + 1}{4R_{SS}}\right)\rho^2 + R_{ss} \quad (1)$$

where γ is a flaring parameter and R_{ss} is the subsolar magnetopause distance [*Belenkaya et al.*, 2005]. Any value of $\gamma > 1$ is physically unreasonable, because it gives a subsolar standoff distance that is not the minimum distance between the magnetopause and the planet. Setting $\gamma = 1$, we find $R_{ss} = 1.25\ R_M$ as the best fit paraboloid. This model does not provide a good visual fit, however, to data either on the dayside or in the distant tail region. Relaxing the constraint of $\gamma > 1$ gives a better fit to the crossings on the nightside, but the resulting model still does not fit the dayside points. We find that the paraboloid model represents the dayside magnetopause shape best when we exclude the tail crossings, yielding $R_{ss} = 1.5\ R_M$ and $\gamma = 1$ (Figure 3).

[22] We also fit the magnetopause crossings with the functional form proposed by *Shue et al.* [1997] (hereafter referred to as the Shue et al. model) and given by

$$R = \sqrt{X^2 + \rho^2} = R_{ss}\left(\frac{2}{1 + \cos\theta}\right)^{\alpha} \quad (2)$$

where R is the distance from the dipole center, $\theta = \tan^{-1}\left(\frac{\rho}{X}\right)$, and α is another flaring parameter that governs whether the magnetotail is closed ($\alpha < 0.5$) or open ($\alpha \geq 0.5$). This model has been used successfully to model the Earth's magnetopause [*Shue et al.*, 1997, 2000] as well as the magnetopause of other planets, such as Saturn [*Arridge et al.*, 2006]. The Shue et al. model that best fits our midpoint magnetopause crossings yields parameter values of $R_{ss} = 1.45\ R_M$ and $\alpha = 0.5$ (shown in Figure 3). As can be seen from Figure 3, the Shue et al. model provides a better representation of the magnetopause crossings than the paraboloid model. Even for the Shue et al. model, the best fit parameters are not tightly constrained, as similar RMS values are achieved over a range of values for R_{ss} and α (Figure 4). This behavior is in part because of a trade-off between the R_{ss} and α parameters, imposed by the observation geometry, and in part because of the spread in the magnetopause crossing positions most likely caused by dynamics of variable solar wind and IMF conditions. To better constrain our best fit parameters, we conducted analyses of the residuals (the perpendicular distance of our

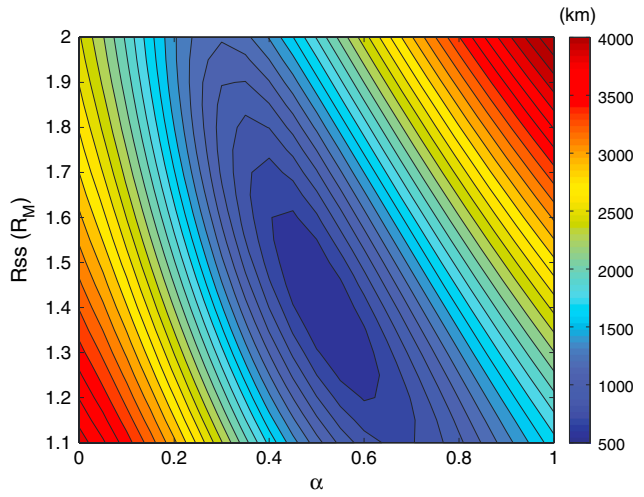

Figure 4. RMS misfit between the midpoints of the magnetopause crossings and the Shue et al. model, as a function of the subsolar standoff distance R_{ss} and the flaring parameter α.

crossings from the model boundary) for a range of models with R_{ss}-α parameter pairs from the minimum misfit region in Figure 4. We find that as we depart from the best fit parameters on either side of the misfit well, the residuals have distributions with a nonzero mean and are not Gaussian. Thus, even though the RMS misfit is not very different from the absolute minimum value in the minimum misfit region, the models generated by the parameter pairs in that region describe the data less well than our best fit model. In addition, models have residuals that vary systematically with X_{MSO}. This situation can be visualized by taking, for example, a model curve lying within the minimum misfit region with $R_{ss} = 1.25\ R_M$ and $\alpha = 0.6$. Such a boundary yields residuals that are systematically positive on the dayside (i.e., the boundary is too close to the planet relative to the observations) and are systematically negative on the nightside (i.e., the boundary is too flared and farther from the planet on average than the data). On the other hand, the residuals of the best fit model with $R_{ss} = 1.45\ R_M$ and $\alpha = 0.5$ have zero mean and a Gaussian distribution and show no systematic variation with X_{MSO}. Also, the RMS misfit (~590 km) for the best fit Shue et al. model is a factor of 1.5 lower than that of the best-fit paraboloid model (which was fit only to the dayside data), and thus, we use only the Shue et al. curve to model the magnetopause for the remainder of this discussion.

3.1.2. Bow Shock

[23] To characterize the shape of the bow shock, the midpoints of the bow shock crossings were modeled by a conic section given by *Slavin et al.* [2009]:

$$\sqrt{(X - X_0)^2 + \rho^2} = \frac{p\varepsilon}{1 + \varepsilon \cdot \cos\theta} \tag{3}$$

where the focus of the conic section lies at X_0 along the line through the planetary dipole that parallels the X axis at X_0. The focus point X_0, the eccentricity ε, and the focal parameter p (which together with the eccentricity gives the semi-latus rectum $L = p\varepsilon$) are determined by a grid search method that minimizes the RMS misfit. The best-fit parameters to the bow shock midpoints are given by $X_0 = 0.5\ R_M$, $\varepsilon = 1.04$, and $p = 2.75\ R_M$ (Figure 5). As mentioned above, bow shock identification is difficult for parallel bow shock conditions, and the outliers in bow shock locations are due to the conservative outer limits chosen for crossings during these conditions. Our best-fit model has an RMS misfit of ~1100 km between model boundary and bow shock position. The extrapolated nose distance for this best-fit model is 1.90 R_M, which yields an approximate magnetosheath thickness of 0.45 R_M from our midpoint magnetopause and bow shock fits. This magnetosheath thickness is comparable to that predicted at Mercury by magnetohydrodynamic and hybrid models [e.g., *Benna et al.*, 2010; *Müller et al.*, 2012].

3.2. Probabilistic Fits

[24] We also examined the magnetopause and bow shock positions in a probabilistic manner, by means of a method employed at Jupiter by *Joy et al.* [2002]. As described in section 2, for each crossing we identified an extended region in space within which the magnetopause or bow shock crossings occurred. The inner and outer limits of the boundaries that we identified span the portion of the spacecraft trajectory over which boundary encounters occurred during each pass. The data set therefore reflects locations where encounters with the magnetopause and bow shock boundary were probable, and so we used the crossing data to build a probability density map of these boundaries around the planet. The spacecraft trajectories between each inner and outer crossing limit were registered on spatial grids around the planet, and the number of crossings passing through each grid cell was used to build a probability density map of the region of space in which the magnetopause and bow shock are most likely to be encountered.

[25] We divided space around the planet into grid cells as follows. For the magnetopause, we adopted a spherical

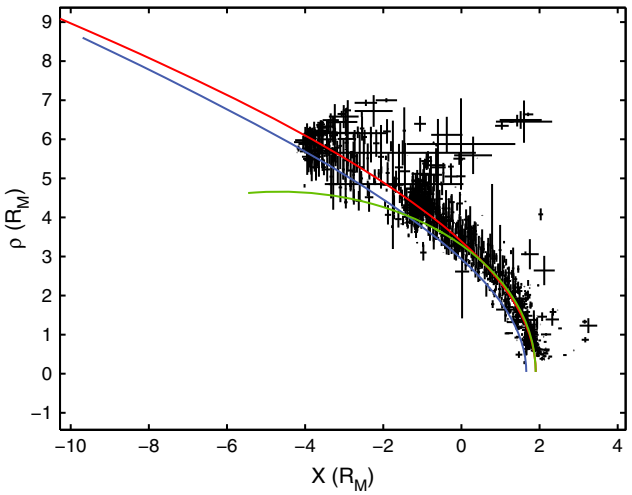

Figure 5. Midpoints between the inner and outer bow shock crossing positions. Error bars show the distance between the inner and outer crossings. Curves show the best-fit conic section to the data (red) and models from previous studies by *Slavin et al.* [2009] (blue) and *Russell* [1977] (green). Parameters for the best-fit model to the bow shock midpoints are $p = 2.75\ R_M$, $\varepsilon = 1.04$, and $X_0 = 0.5\ R_M$.

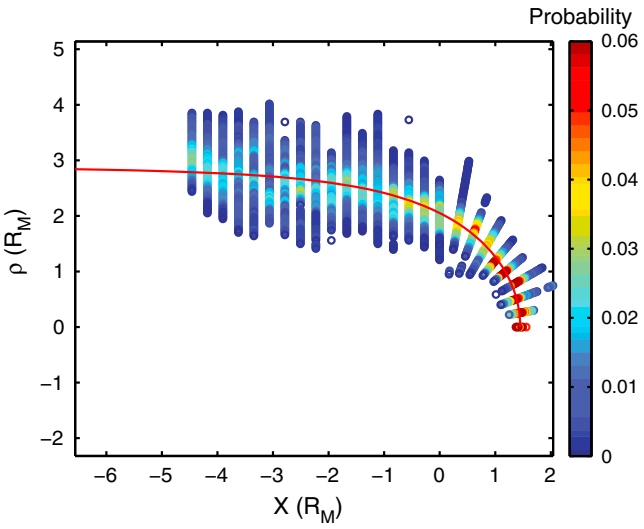

Figure 6. Probability density map of aberrated magnetopause positions. The white space represents regions where the magnetopause is never observed, the blue regions where it is very rarely observed, and the dark red regions where it is observed most often. The red line represents the Shue et al. model that best fits the probability densities, with $R_{ss} = 1.45\ R_M$ and $\alpha = 0.5$. The probabilities sum to 1 along each X bin on the nightside and along each θ bin on the dayside.

coordinate system on the dayside and a cylindrical system on the nightside to match approximately the shape of the boundary. The dayside was split into cells in r_{MP}, θ_{MP}, and ϕ_{MP}, where $r_{MP} = \sqrt{(X^2 + \rho^2)}$ is the distance from the dipole center, $\theta_{MP} = \cos^{-1}(X/r_{MP})$ is the angle measured from the axis of revolution, and ϕ_{MP} is the azimuth about the axis of revolution defined as $\tan^{-1}[Y/(Z - Z_d)]$. Grid cells were spaced every 50 km, 10°, and 30° in r_{MP}, θ_{MP}, and ϕ_{MP}, respectively. The nightside was divided into grid cells spaced every 50 km, 680 km, and 30° in ρ, X, and ϕ_{MP}, respectively. Because the bow shock nightside data were not well matched by a cylindrical shape, we used the spherical coordinate system, r_{SK}, θ_{SK}, ϕ_{SK}, but with an origin on the axis of revolution at $X = -4\ R_M$ for all of the bow shock crossings. That is, $r_{SK} = \sqrt{((X + 4R_M)^2 + \rho^2)}$, $\theta_{SK} = \cos^{-1}[(X + 4R_M)/r_{SK}]$, and $\phi_{SK} = \phi_{MP}$. The bow shock bins were 50 km, 5°, and 30° in r_{SK}, θ_{SK}, and ϕ_{SK}, respectively. These coordinates are used only to bin the data, and all results are shown in ρ-X space.

[26] We evaluated the frequency with which the spacecraft trajectory between the inner and outer magnetopause (or bow shock) crossings passed through each bin. That is, for each orbit, each grid cell received a "hit" for every 1 s measurement point in that bin between the inner and outer limit of the magnetopause (or bow shock). The hits were summed in each cell over all orbits for the magnetopause and bow shock boundaries separately. The cells with the highest number of hits had the highest likelihood of falling between the inner and outer boundary limits. Probabilities were evaluated by dividing the number of counts in each cell by the sum of all the hits in all cells along a predefined direction (e.g., along each X bin on the nightside and along each θ bin on the dayside for the magnetopause). The normalization choice reflects the 100% probability that the boundary occurs at some X or θ position. This procedure resulted in three-dimensional (3-D) probability density maps of both the magnetopause and bow shock around the planet. For the analyses that follow, we assumed that both the bow shock and magnetopause are figures of revolution. We used a two-dimensional (2-D) probability distribution in the ρ-X plane generated by summing the hits in bins with the same r and θ (dayside) or ρ and X (nightside), over all ϕ bins and then normalizing by the total number of counts along r (or ρ) at each θ (or X). The assumption of a figure of revolution for each boundary was tested quantitatively (see section 5).

[27] The 2-D probability density map (Figure 6) for the magnetopause shows that this boundary has a maximum probability of occurrence that lies within a narrow band on the dayside and within a more extended region on the nightside. We fit Shue et al. models to this probabilistic boundary by performing a weighted fit to the grid cell locations in ρ-X space, such that each cell location was weighted by its probability. The best-fit curve yielded the same model parameters as the fit to the magnetopause midpoints (Table 1), but with a lower RMS misfit of ~96 km that reflects the use of the probabilities as weights.

[28] The bow shock probability density map (Figure 7) shows a more extended spread in the boundary locations than that for the magnetopause, in particular on the nightside, where the highest-probability regions occur at large ρ values. This spread is the result of outlier crossings (Figure 5), most of which occurred during parallel shock

Table 1. Summary of the Best-Fit Shue et al. Model Parameters to the Magnetopause Crossing Points Under Different Ram Pressure Conditions for a Fixed α Value of 0.50.

	Midpoint Fit			Probabilistic Fit		
	R_{ss} (R_M)	α	RMS Residual (km)	R_{ss} (R_M)	α	RMS Residual (km)
All P_{Ram}	1.45	0.50	587	1.45	0.50	96
P_{Ram} corrected	–	–	–	1.45	0.50	94
$<P_{Ram}>$ = 8.8 nPa[a]	–	–	–	1.55	0.50	96
$<P_{Ram}>$ = 11.5 nPa	–	–	–	1.5	0.50	106
$<P_{Ram}>$ = 15.2 nPa	–	–	–	1.45	0.50	155
$<P_{Ram}>$ = 18.8 nPa	–	–	–	1.4	0.50	120
$<P_{Ram}>$ = 21.6 nPa	–	–	–	1.35	0.50	115

[a]Brackets denote mean value within each ram pressure bin.

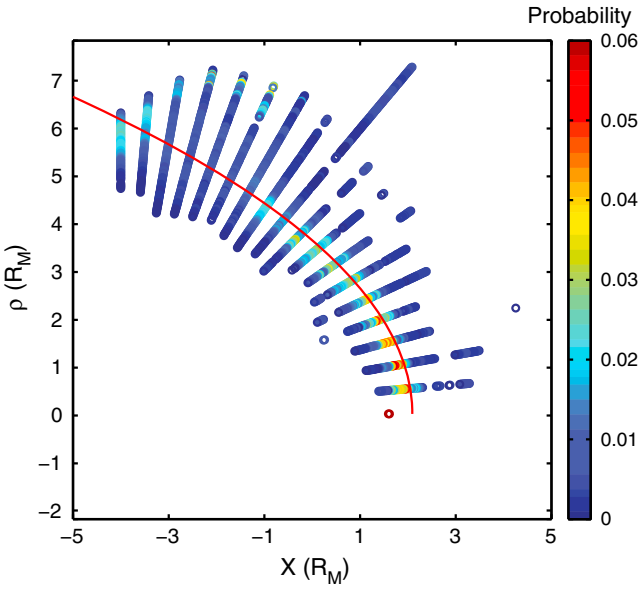

Figure 7. Probability density map of the aberrated bow shock crossings. The red line represents the best-fit conic section to the probability densities, with $p = 3.2\ R_M$, $\varepsilon = 0.99$, and $X_0 = 0.5\ R_M$. The probabilities sum to 1 along each X bin on the nightside and along each θ bin on the dayside.

conditions. A conic fit to the grid cell locations weighted by the probabilities yields slightly different model parameters than our midpoint fit. The least sensitive of the model parameters in our fits was the focus location, X_0: varying this parameter from $-0.7\ R_M$ to $0.7\ R_M$ changed the RMS misfit by only a few percent. Due to the covariance between the parameters, this variation in X_0 was accompanied by large changes in p and ε, and the bow shock shape varied from an ellipse to an open hyperbola, but the RMS misfit changed only by a few percent. We thus fixed the focus location to $X_0 = 0.5\ R_M$ in order to establish best-fit p and ε values that yielded bow shock shapes as close to hyperboloids as possible. The fit parameters to the bow shock were then given by $X_0 = 0.5\ R_M$, $\varepsilon = 0.99$, and $p = 3.2\ R_M$, with a weighted RMS misfit of ~187 km (Table 2). With these parameters, the bow shock nose distance is extrapolated to be $2.09\ R_M$, which gives a magnetosheath width of $0.64\ R_M$ from the probabilistic analysis. The shock distance from the dipole-Sun line in the Y-Z plane is given by $3.83\ R_M$ at $X = 0$ and by $6.35\ R_M$ at $X = -4\ R_M$.

4. Response of Boundaries to Solar Wind Forcing

4.1. Magnetopause

[29] The magnetopause shape and location are expected to vary with solar wind and IMF conditions [e.g., *Fairfield*, 1995; *Shue et al.*, 2000]. Figure 8 shows the solar wind statistics at Mercury at the time of the bow shock crossings, obtained from averages of MESSENGER MAG observations of the IMF and from ENLIL model predictions of the solar wind density, speed, ram pressure, and Alfvén Mach number [*Odstrcil*, 2003; *Baker et al.*, 2013]. We assumed that these statistics held at the times of both the magnetopause and bow shock crossings on a given orbit and used them to examine the response of the boundaries to the IMF and solar wind.

[30] The magnetopause boundary is observed to be closer to the planet during times of increased ram pressure and farther out during times of low ram pressures (Figure 9). *Baker et al.* [2013] showed that solar wind ram pressure values from the ENLIL model order and organize the magnetopause standoff distance. This behavior is expected, because the magnetic pressure of the planet's magnetosphere and the solar wind dynamic pressure are the two largest contributors to the pressure balance that defines the magnetopause boundary. The ram pressure effect is the dominant factor influencing the magnetopause, because any IMF effects, if present, were not readily apparent in the raw data. We thus investigated any possible effect of the IMF direction on the magnetopause after removing the dependence on P_{Ram}.

[31] We assessed changes in the magnetopause shape and position under different ram pressure conditions. We binned the magnetopause crossing data into five P_{Ram} bins, such that each P_{Ram} bin contained one fifth of the range of P_{Ram} values represented in the data. Thus, the P_{Ram} bins did not contain equal numbers of data points, but the range of P_{Ram} values was the same in each bin. We built 2-D probability density maps for each P_{Ram} bin and conducted fits of the two-parameter Shue et al. model to these separately. The largest uncertainty in the best-fit model shape is most likely associated with the highest ram pressure bin, which includes the more extreme solar events that may not be properly

Table 2. Summary of the Best-Fit Conic Section Parameters to the Bow Shock Crossings Under Different Mach Number Conditions

	Midpoint Fit[a]					Probabilistic Fit[a,b]				
	X_0 (R_M)	p (R_M)	ε	RMS Misfit (km)	Subsolar Distance (R_M)	X_0 (R_M)	p (R_M)	ε	RMS Residual (km)	Subsolar Distance (R_M)
All M_A	0.5	2.75	1.04	1115	1.90	0.5	3.20	0.99	187	2.09
M_A corrected	–	–	–	–	–	0.5	2.90	1.02	149	1.96
$<M_A> = 4.12$[c]	–	–	–	–	–	0.5	3.55	1.02	241	2.29
$<M_A> = 6.32$	–	–	–	–	–	0.5	2.95	1.02	195	1.99
$<M_A> = 11.8$	–	–	–	–	–	0.5	2.75	1.02	162	1.89
Low cone angle ($\theta < 45°$)	–	–	–	–	–	0.5	3.10	0.99	169	2.04
High cone angle ($\theta > 45°$)	–	–	–	–	–	0.5	2.95	0.99	157	1.97

[a]In the fits, X_0 was fixed at a value of $0.5\ R_M$ (see text).
[b]In the fits to the three different M_A bins, p was the only parameter varied, and ε was fixed at the mean value between the best-fit probabilistic and best-fit midpoint result (see text).
[c]Brackets denote mean M_A value within each Mach number bin.

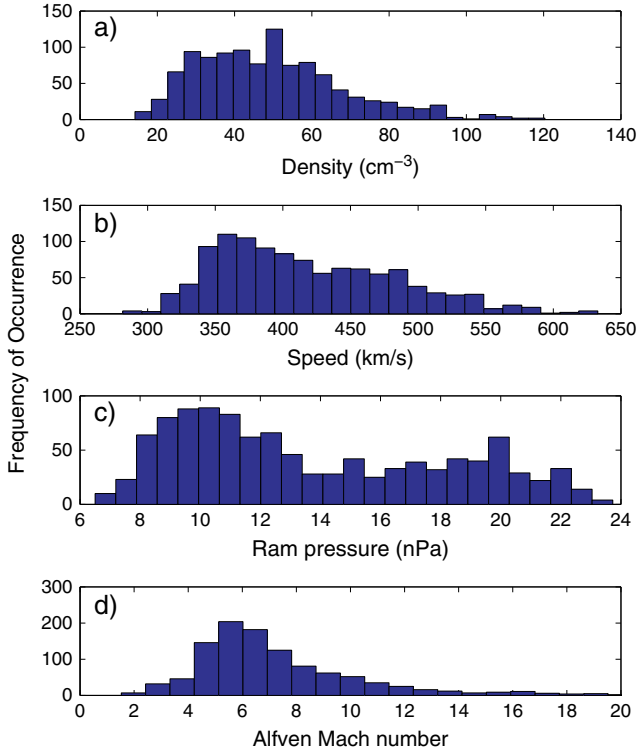

Figure 8. Solar wind statistics at the times of the bow shock crossings obtained from ENLIL model predictions of the solar wind and from averages of MESSENGER MAG observations in the interplanetary medium for the IMF. Histograms of (a) solar wind number density (cm^{-3}), (b) solar wind speed (km s^{-1}), (c) solar wind ram pressure (nPa), and (d) solar wind Alfvén Mach number. In Figure 8d, 15 observations with Mach numbers > 20 are not shown; these numbers reach a maximum value of 69.0.

captured by the ENLIL model. The R_{ss} and α values for the best-fit curves for each of the ram pressure bins are plotted in Figure 10. With the exception of the highest P_{Ram} bin, the R_{ss} parameter decreases overall with P_{Ram}; in contrast, α shows no systematic variation with P_{Ram}. Thus, we first removed the dominant R_{ss} versus P_{Ram} variation from the data and normalized the magnetopause crossings by the ram pressure. To do this, we estimated only the R_{ss} parameter for the data in each of the five P_{Ram} bins while keeping α fixed at its average best-fit value of 0.5 (i.e., a fixed magnetopause shape). We checked that the best-fit models for the fixed-α fits in all the five P_{Ram} bins yielded residuals that had Gaussian distributions with a nearly zero mean. The R_{ss} values for the best-fit curves for each of these ram pressure bins are plotted in Figure 11 and given in Table 1. These were fit by a power law given by $R_{ss} = (2.15 \pm 0.10)\, P_{Ram}^{[(-1/6.75)\pm\ 0.024]}$, where R_{ss} is in units of R_M and P_{Ram} in nPa and the uncertainties are the 95% confidence limits on the exponent and the coefficient obtained from the fitting procedure. The magnitude of the exponent is only slightly less than the $-1/6$ dependence of R_{ss} on P_{Ram} expected for a simple pressure balance between the internal dipole magnetic field pressure (and small internal plasma pressure) and solar wind dynamic pressure. This result suggests that the effects of induction in Mercury's conductive interior, which "stiffens" the dayside magnetosphere against changes in solar wind pressure [*Seuss and Goldstein*, 1979; *Goldstein et al*., 1981; *Grosser et al*., 2004; *Glassmeier et al*., 2007], may be present, but if so it is a secondary effect, at least at the altitudes over which MESSENGER samples the magnetopause. A detailed study of induction signatures is beyond the scope of this paper. Refinement of the power law above will require both additional observations and assessment of uncertainties in the ENLIL model predictions.

[32] The power law relationship above indicates that a ram pressure of 175 nPa would collapse the magnetopause to the planet's surface. We note that the minimum and maximum pressures consistent with the uncertainties in our power law fit span a wide range from 65 and 692 nPa. In the simulations conducted by *Kabin et al*. [2000], a ram pressure of 147 nPa was found to collapse the magnetopause to the surface, which is within our uncertainty range. Using a $-1/6$ power law (i.e., the relation expected in the absence of induction) relative to the mean observed R_{ss} of 1.45 R_M yields a lower pressure for the collapse of the magnetosphere of 133 nPa, well within the range of uncertainty of our power law expression.

[33] With the derived power law relationship, we normalized our magnetopause crossings as follows. From the ENLIL data, we found the corresponding P_{Ram} value for the inbound and outbound portion of each orbit, and from those values we established an associated R_{ss} value for each orbit from the power law fit to our P_{Ram}-binned data. The ram-pressure-independent magnetopause crossing locations were then determined by multiplying the X, Y, and $(Z - Z_d)$ values by the mean R_{ss} for all crossings (i.e., $R_{ss} = 1.45$ R_M) divided by the R_{ss} value associated with each observation point. Figure 12 shows the probability density map of the magnetopause after the solar wind ram pressure dependence was removed. The P_{Ram}-independent magnetopause location is better constrained than the uncorrected locations

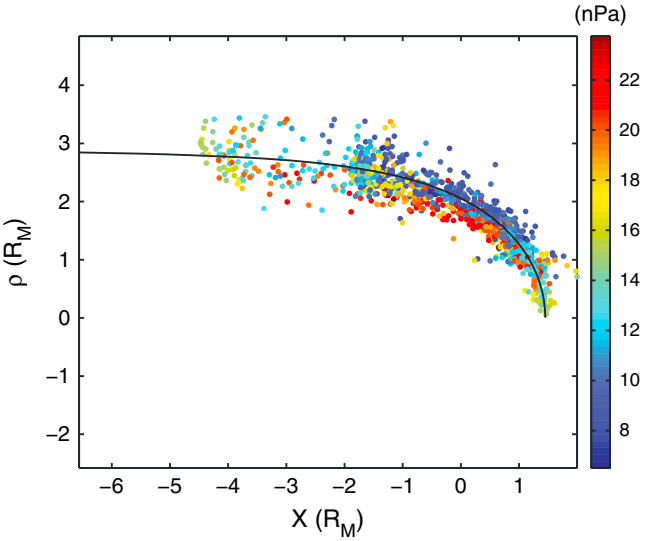

Figure 9. Midpoints of the magnetopause crossings color coded by solar wind ram pressure. The solid black line through these data points is the best-fit Shue et al. model. During times of high solar wind ram pressure, the magnetopause is observed to move closer to the planet, as expected.

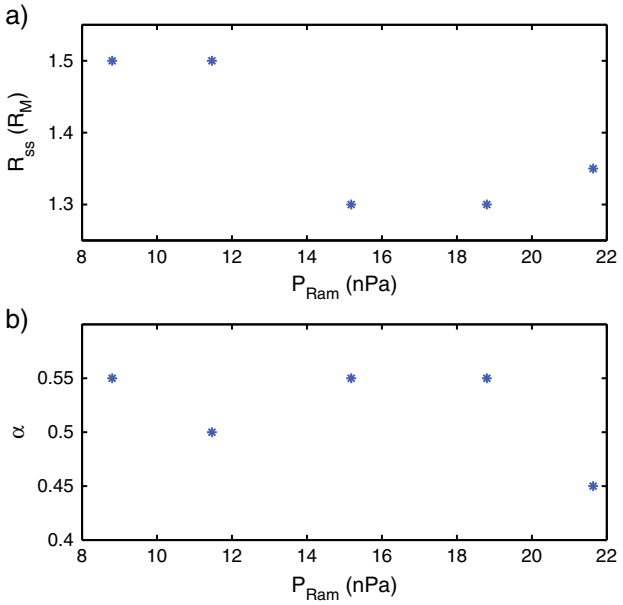

Figure 10. (a) Magnetopause subsolar standoff distance R_{ss} plotted as a function of solar wind ram pressure when both parameters were allowed to vary in the Shue et al. model fits. The blue stars represent R_{ss} values established from best-fit curves to five ram-pressure data bins. (b) Flaring parameter α corresponding to the R_{ss} values in Figure 10a for the best-fit Shue et al. curves, plotted as a function of solar wind ram pressure.

(Figure 6), especially on the dayside, where the zones of high-probability regions lie in a narrow band. Although the model that best fits these data is still described by the same parameters as the P_{Ram}-uncorrected magnetopause (see Table 1), the RMS residual is lower than for the P_{Ram}-uncorrected crossings, with a value of ~94 km. A statistical F test shows that at the 91% significance level the variance of the P_{Ram}-corrected magnetopause model is lower than the variance of the P_{Ram}-uncorrected magnetopause model.

[34] After removing the first-order variation of the magnetopause position with ram pressure, we binned the data again into the same P_{Ram} bins as above, fixed R_{ss} to the best-fit P_{Ram}-corrected value of 1.45 R_M and left α to vary in *Shue et al.* model fits to these bins to test the influence of ram pressure on the flaring of the magnetopause. Unlike the situation at Earth, there is no increase in flaring of the magnetopause with increased ram pressure. This result is expected if the magnetospheric currents and the ratio of the static solar wind pressure to the dynamic pressure remain constant [*Coroniti and Kennel*, 1972].

[35] We then assessed whether the IMF direction affects the magnetopause shape after the ram pressure dependence was removed. Since the MESSENGER IMF averages 1 h upstream of the bow shock are not ideal for evaluating IMF B_Z affects on the magnetosphere [*Winslow et al.*, 2012], we used the magnetic shear angle across the magnetopause to search for any overall dependence on magnetic reconnection. The magnetic shear was calculated by taking the dot product of the magnetic field unit vector 1 min inside the inner edge of the magnetopause crossing and the unit vector 1 min outside the outer edge of the magnetopause crossing. Figure 13 shows the distribution of magnetic shear angles across the magnetopause. The magnetic shear angle distribution is peaked at ~90°, reflecting the mainly antisunward or sunward IMF at Mercury and the dominantly northward planetary field on the dayside. The number of events for low shear (below ~45°) and high shear (above ~135°) angles are quite low and do not provide sufficient cases to evaluate magnetopause shape fits under these contrasting conditions. We note that our average magnetopause boundary corresponds to substantial magnetic shear conditions, so some influence of reconnection is likely reflected in our time-averaged descriptions of the magnetopause shape and size.

4.2. Bow Shock

[36] We used ENLIL model data as well as MESSENGER IMF averages to assess how the bow shock is affected by solar wind and IMF conditions. To first order, the solar wind Alfvén Mach number is the dominant factor affecting the bow shock; the shock is closer to the planet during high M_A than during low M_A (Figure 14). This result is expected and in agreement with gas dynamic and magnetohydrodynamic simulations [*Spreiter and Stahara*, 1985; *Benna et al.*, 2010; *Müller et al.*, 2012]. As M_A increases, the jump of the plasma flow speed transverse to the shock surface also increases, corresponding to higher plasma flow speed around the magnetopause that results in a thinner magnetosheath [*Spreiter and Stahara*, 1980]. At greater downstream distances, the bow shock weakens as it asymptotically approaches its Mach cone [*Slavin et al.*, 1984; *Verigin et al.*, 2003b]. Although MESSENGER does not sample the bow shock at large downstream distances, an enhanced flaring of this surface with decreasing Mach number may be present (Figure 14).

[37] To establish the bow shock position normalized by Alfvén Mach number, we adopted a procedure to remove the Mach number dependence similar to that applied to the magnetopause to remove the dependence on ram pressure. We binned the bow shock crossings into three M_A bins and fit separate conic sections to each. To have sufficient

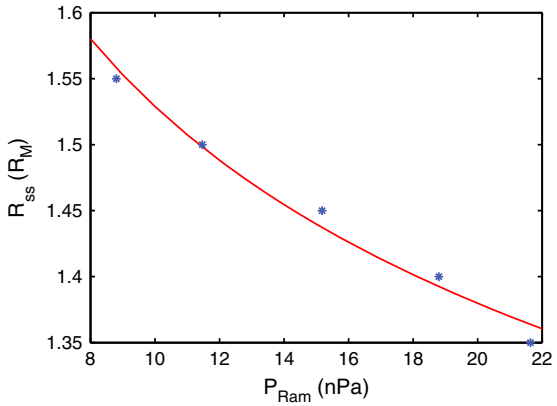

Figure 11. Magnetopause subsolar standoff distance, R_{ss}, plotted as a function of solar wind ram pressure for fits when the flaring parameter was kept fixed at a value of 0.5. The blue stars represent R_{ss} values established from best-fit curves to five ram pressure data bins, and the red curve is a power law fit to these values with an exponent of -0.148 ± 0.024.

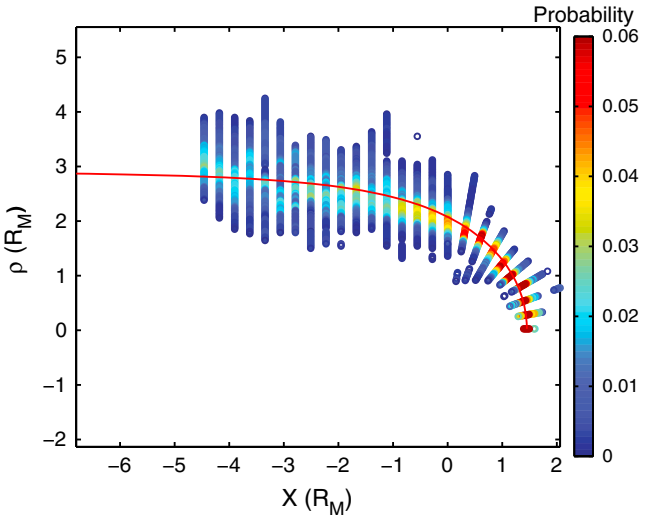

Figure 12. Probability density map of the aberrated magnetopause crossings after the crossing positions were normalized by solar wind ram pressure. The best-fit Shue et al. model (red curve) yields the same R_{ss} and α values as before (Figure 6), but the spread in the data has decreased somewhat on the dayside, and the regions of highest probability are more spatially constrained.

data points in each M_A bin to perform model fits (see Figure 8d), the low-M_A bin was assigned $M_A < 5$, the medium-M_A bin had values in the range $5 < M_A < 8$, and the high-M_A bin had values of $M_A > 8$ (see Table 2 for mean values of M_A in each bin). Fits in which all three bow shock parameters were varied revealed large trade-offs among the three model parameters, in a manner similar to the magnetopause fits. However, through these fits we were able to establish that the parameter most systematically affected by M_A is the focal parameter p, which steadily decreased with increasing M_A. The other two parameters did not show any systematic behavior with M_A. Thus, in order to normalize our bow shock boundary by M_A and look for higher-order dependencies in the data, we assumed that the bow shock shape does not change (by keeping X_0 and ε fixed at their average values) and fit separate conic sections to the bow shock crossings in the three M_A bins. We again checked that these fixed-shape fits still yielded residuals with zero means and nearly Gaussian distributions. In our fits, the low-M_A bin had the highest RMS misfit, and the high-M_A bin had the lowest RMS misfit for all the fits conducted (Table 2), consistent with most of the spread in the bow shock location occurring during low M_A (Figure 14). From the fits of conic sections to the different M_A bins, we established a power law relationship between p and M_A, given by $p = (4.79 \pm 2.54)\ M_A^{(-0.23 \pm 0.17)}$, where the uncertainties in the exponent and coefficient are the 95% confidence limits determined from the fitting procedure. We scaled the bow shock crossing positions by p_0/p_i, where p_0 is the mean p value obtained from averaging the p values from the midpoint and probabilistic fit (Table 2), and p_i is the p parameter for the i^{th} crossing point determined from the power law relationship above. The resulting probability density map for the M_A-corrected bow shock positions (Figure 15) shows a decrease in the spread of the bow shock locations, as well as a marked decrease in the distance between the high-probability regions on the nightside and the best-fit model boundary. The best-fit model boundary to the M_A-independent bow shock crossings has a p parameter of 2.9 R_M, an eccentricity of 1.02, a focus point of $X_0 = 0.5$, and a minimum RMS misfit ~20% less than that for the fit shown in Figure 7.

[38] We also assessed the influence of M_A on the flaring of the bow shock after removing the first-order dependence of the bow shock position on the Mach number. By allowing ε to vary (and fixing $X_0 = 0.5$ and $p = 2.9\ R_M$) in our conic sections fit to the different M_A bins, we found no statistically significant variation of ε with M_A. For the sake of completeness, we also conducted similar tests at a variety of other X_0

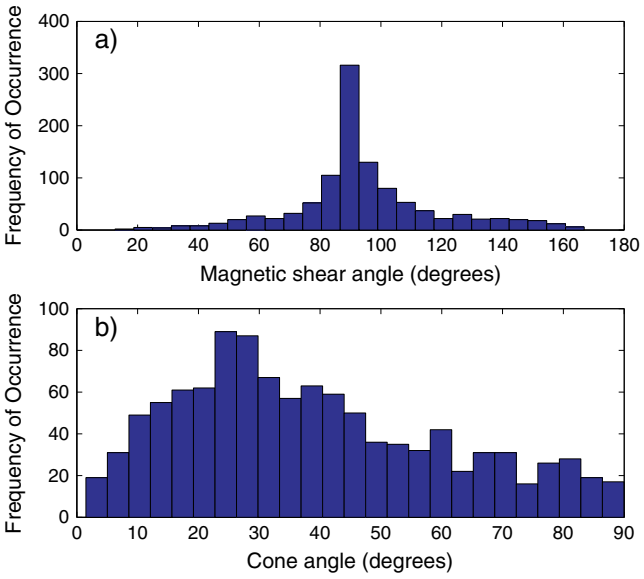

Figure 13. Histograms of (a) the magnetic shear angle across the magnetopause and (b) the IMF cone angle, calculated from MESSENGER magnetic field data.

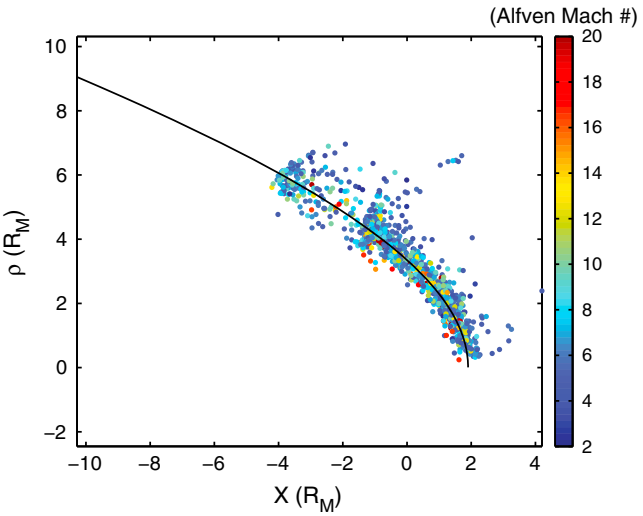

Figure 14. Midpoints of the bow shock crossings color coded by solar wind Alfvén Mach number. The solid black line through the data is the conic section best fit to the midpoints.

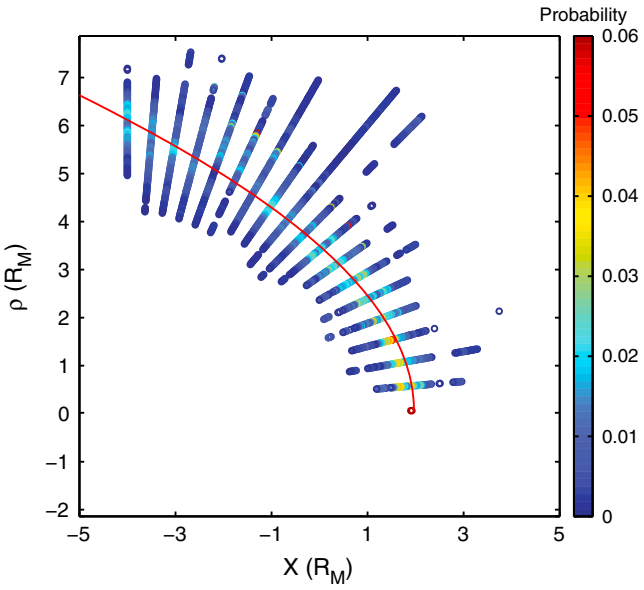

Figure 15. Probability density map of the aberrated bow shock crossings after removing the dependence on Alfvén Mach number. The red line represents the best-fit conic section to the probability densities, with $p = 2.9$ R_M, $\varepsilon = 1.02$, and $X_0 = 0.5$ R_M. The normalized bow shock is more spatially constrained, in a manner similar to that for the magnetopause normalized by ram pressure.

values, which yielded similar results. We conclude that variation in bow shock flaring with M_A is masked by the high variability of the crossing locations. More bow shock crossings are needed at high M_A values to establish whether ε varies systematically with M_A at Mercury.

[39] The IMF cone angle is also expected to affect the bow shock, as the shock is anticipated to flare during quasi-parallel shock conditions [*Greenstadt*, 1991]. We evaluated whether any dependence on IMF cone angle is observed in the bow shock location or shape after the Mach number dependence was removed. The IMF cone angle is given by $\theta = \cos^{-1}\left(\frac{|B_X|}{B_{\text{Total}}}\right)$, and its distribution is shown in Figure 13. By dividing the data into bins of low ($\theta < 45°$) cone angle and high ($\theta > 45°$) cone angle, we found that there is no resolvable difference between conic section fits to the bow shock locations separated by cone angle (Table 2). The shock is more spatially spread out for the low-cone-angle bin, an expected result because a low cone angle signifies parallel shock conditions. The flaring of the bow shock does not appear to be affected by IMF cone angle.

5. Discussion

[40] The observations of Mercury's magnetopause and bow shock presented here indicate that these boundaries are variable and dynamic. At Mercury, the solar wind ram pressure and the Alfvén Mach number are the two dominant external influences on the boundaries. The magnetopause is observed to move planetward during high P_{Ram}, and similarly the bow shock moves planetward during times of high M_A. Unlike at Earth, increased P_{Ram} does not increase the flaring of the magnetopause; the shape of the boundary is unchanged under variations in solar wind ram pressure. In a like manner, M_A does not appear to influence the flaring of the bow shock at Mercury despite the fact that at Earth the shock is more flared during times of low M_A.

[41] An important result is that the average magnetopause becomes cylindrical at relatively small downstream distances of only ~2–3 R_M (Figure 3). At Earth, in contrast, the magnetotail does not cease flaring until a downstream distance of ~100 R_E [*Slavin et al.*, 1983b]. Expressed in terms of subsolar magnetopause standoff distances, the downstream flaring of Mercury's tail ceases by ~2 R_{ss} whereas at Earth this effect is not seen until ~10 R_{ss}. The factors determining the location where tail flaring ceases are not well understood, but the position likely corresponds to the distance at which the plasma sheet is disconnected from the planet as a result of reconnection, and plasma flow in the tail is all antisunward. At Earth this position occurs at about −100 R_E [*Zwickl et al.*, 1984], whereas for Mercury *Slavin et al.* [2012a] estimated a downstream distance of ~3 R_M from MESSENGER flyby observations of reconnection in the tail. Mercury's magnetopause is well fit by the Shue et al. model with $\alpha = 0.5$, which defines the transition from an open ($\alpha > 0.5$) to a closed ($\alpha < 0.5$) magnetospheric cavity on the nightside. From the best-fit Shue et al. model for the ram-pressure-corrected magnetopause we find that the magnetotail is on average nearly cylindrical with a radius of 2.05 R_M at the dawn-dusk terminator and 2.77 R_M at a distance of 4 R_M down the tail. In comparison, Earth's magnetopause is more flared, with the data fit well by Shue et al. models that have $\alpha > 0.5$ [*Shue et al.*, 1997].

[42] The analysis of the magnetopause and bow shock boundaries in ρ-X space was based on the assumption of rotational symmetry about the dipole-Sun line. We tested whether this assumption was justified both qualitatively and quantitatively. First, the boundary crossings plotted in X-Y and X-$(Z - Z_d)$ space did not reveal systematic differences. The ram pressure and Mach number are not observed to cause any asymmetries in the shape, as the boundary crossings corrected for P_{Ram} and M_A have similar shapes to the uncorrected crossings in X-Y and X-$(Z - Z_d)$ space. These comparisons indicate that variations from rotational symmetry can be treated as a perturbation to the figures of revolution. We then assessed the degree to which systematic deviations from figures of revolution are present. From the corrected crossing locations, we evaluated the best-fit models for both boundaries, and we calculated the perpendicular distances of each crossing from the model boundaries as a function of the azimuthal angle, i.e., ϕ_{MP} or ϕ_{SK}. If either the magnetopause or bow shock were flattened or elongated in the north-south direction, such an effect would be evident as a sinusoidal variation in ϕ_{MP} or ϕ_{SK}, respectively, relative to the mean boundary at a period of 180°, i.e., two cycles. We did not observe any systematic departures from figures of revolution for either the magnetopause or the bow shock. By binning the deviations into 2° bins in ϕ_{MP} or ϕ_{SK} and fitting a sinusoid to these binned deviations, we find maximum sine wave amplitudes of 62 and 3 km for the magnetopause and bow shock, respectively. These sine wave amplitudes are more than an order of magnitude smaller than the variability in the deviations of the two boundaries about the models. We conclude that,

to first order, the boundaries are figures of revolution. The scatter relative to the mean is high, however, implying that dynamic variability in Mercury's magnetosphere and bow shock are large and that second-order structure could be present but masked by the large dynamic variability. It is thus possible that instantaneously these boundaries are not figures of revolution. However, on average, the departures from figures of revolution are small compared with the dynamics in the system. Because of the high variability of the crossing locations analyzed so far, we cannot yet resolve any average asymmetries in the boundary shapes. At Earth, the maximum departure from a figure of revolution at high latitudes is ~1 R_E [*Lu et al*., 2011], which corresponds to ~0.1 R_{ss} (subsolar standoff distance is ~10 R_E). In comparison, an equivalent 0.1 R_{ss} departure is only ~350 km at Mercury, which would be a sufficiently small departure to be easily masked by the variability in the available data. Such signatures may be resolved with additional observations.

6. Conclusions

[43] We have established Mercury's time-averaged magnetopause and bow shock location and shape from MESSENGER Magnetometer data obtained during 3 Mercury years in orbit. We find that the magnetopause is well described by a Shue et al. model parameterized by a subsolar standoff distance of 1.45 R_M and a flaring parameter of $\alpha = 0.5$. The solar wind ram pressure exerts a primary control on magnetopause location; the boundary moves closer to the planet under higher P_{Ram} (giving a subsolar distance of 1.35 R_M for a mean P_{Ram} of 21.6 nPa) and farther away from the planet under lower P_{Ram} (with an R_{ss} of 1.55 R_M for a mean P_{Ram} of 8.8 nPa), while leaving the shape unchanged (Table 1). The paraboloid model of *Belenkaya et al*. [2005] provides a substantially worse overall fit to the magnetopause crossings than the Shue et al. model, reflecting the absence of evidence for substantial flaring from observations on the nightside. This comparison suggests that future improvements in global models for Mercury's magnetosphere should use a ram-pressure-corrected Shue et al. model magnetopause. The observed low flaring of the magnetotail may imply that magnetic flux has a short residence time in the tail on average. This short residence time of the tail flux could also imply that return convection of flux from the tail to the dayside proceeds rapidly.

[44] The shape of Mercury's bow shock corrected for Alfvén Mach number is that of a hyperboloid given by the parameters $X_0 = 0.5$ R_M, $p = 2.9$ R_M, and $\varepsilon = 1.02$ and a subsolar standoff distance of 1.96 R_M. The bow shock shape does not appear to vary with Alfvén Mach number, as there is no change in flaring. This is an unexpected result, since Earth's bow shock is observed to flare with decreasing Alfvén Mach number. At Mercury, the bow shock moves closer to the planet for high M_A and farther out for low M_A; the extrapolated nose distance of the shock is at 1.89 R_M for a mean M_A of 11.8 and at 2.29 R_M for a mean M_A of 4.12 (Table 2). Both the magnetopause and bow shock boundaries are figures of revolution to first order, but the variability about the mean is large. With the current data available, we do not resolve effects of IMF orientation on the magnetopause or the bow shock. As more data are acquired by MESSENGER under a wider range of external conditions, effects of IMF on the magnetopause or bow shock should be more readily discernible.

[45] The variation of the bow shock and magnetopause location with dynamics is large at Mercury, and understanding the processes that these dynamics reflect is a key area of future study. The derivation of the average boundaries presented here provides a baseline with which to evaluate excursions of the system from its average state. Extensive progress has already been made in understanding boundary waves [*Boardsen et al*., 2010; *Sundberg et al*., 2012] and reconnection at Mercury [*Slavin et al*., 2012a, 2012b; *DiBraccio et al*., 2013]. Extending that work to better understand those aspects of global magnetospheric dynamics that could lead to the large variations in boundary locations is a fruitful area of inquiry.

[46] **Acknowledgments.** The MESSENGER project is supported by the NASA Discovery Program under contracts NAS5-97271 to The Johns Hopkins University Applied Physics Laboratory and NASW-00002 to the Carnegie Institution of Washington. C. L. J. and M. E. P. are supported by MESSENGER Participating Scientist grants NNX11AB84G and NNH08CC05C. R. M. W. and C. L. J. acknowledge support from the Natural Sciences and Engineering Research Council of Canada. We thank the Community Coordinated Modeling Center for providing ENLIL model runs. The authors thank the reviewers for constructive comments.

References

Alexeev, I. I., et al. (2010), Mercury's magnetospheric magnetic field after the first two MESSENGER flybys, *Icarus*, *209*, 23–39, doi:10.1016/j.icarus.2010.01.024.

Anderson, B. J., M. H. Acuña, D. A. Lohr, J. Scheifele, A. Raval, H. Korth, and J. A. Slavin (2007), The Magnetometer instrument on MESSENGER, *Space Sci. Rev.*, *131*, 417–450, doi:10.1007/s11214-007-9246-7.

Anderson, B. J., C. L. Johnson, H. Korth, M. E. Purucker, R. M. Winslow, J. A. Slavin, S. C. Solomon, R. L. McNutt Jr., J. M. Raines, and T. H. Zurbuchen (2011), The global magnetic field of Mercury from MESSENGER orbital observations, *Science*, *333*, 1859–1862, doi:10.1126/science.1211001.

Anderson, B. J., C. L. Johnson, H. Korth, R. M. Winslow, J. E. Borovsky, M. E. Purucker, J. A. Slavin, S. C. Solomon, M. T. Zuber, and R. L. McNutt Jr. (2012), Low-degree structure in Mercury's planetary magnetic field, *J. Geophys. Res.*, *117*, E00L12, doi:10.1029/2012JE004159.

Arridge, C. S., N. Achilleos, M. K. Dougherty, K. K. Khurana, and C. T. Russell (2006), Modeling the size and shape of Saturn's magnetopause with variable dynamic pressure, *J. Geophys. Res.*, *111*, A11227, doi:10.1029/2005JA011574.

Baker, D. N., et al. (2013), Solar wind forcing at Mercury: WSA-ENLIL model results, *J. Geophys. Res. Space Physics*, *118*, 45–57, doi:10.1029/2012JA018064.

Belenkaya, E. S., S. Y. Bobrovnikov, I. I. Alexeev, V. V. Kalegaev, and S. W. H. Cowley (2005), A model of Jupiter's magnetospheric magnetic field with variable magnetopause flaring, *Planet. Space Sci.*, *53*, 863–872, doi:10.1016/j.pss.2005.03.004.

Benna, M., et al. (2010), Modeling of the magnetosphere of Mercury at the time of the first MESSENGER flyby, *Icarus*, *209*, 3–10, doi:10.1016/j.icarus.2009.11.036.

Boardsen, S. A., T. E. Eastman, T. Sotirelis, and J. L. Green (2000), An empirical model of the high-latitude magnetopause, *J. Geophys. Res.*, *105*, 23,193–23,219, doi:10.1029/1998JA000143.

Boardsen, S. A., T. Sundberg, J. A. Slavin, B. J. Anderson, H. Korth, S. C. Solomon, and L. G. Blomberg (2010), Observations of Kelvin-Helmholtz waves along the dusk-side boundary of Mercury's magnetosphere during MESSENGER's third flyby, *Geophys. Res. Lett.*, *37*, L12101, doi:10.1029/2010GL043606.

Caan, M. N., R. L. McPherron, and C. T. Russell (1973), Solar wind and substorm-related changes in the lobes of the geomagnetic tail, *J. Geophys. Res.*, *78*, 8087–8096, doi:10.1029/JA078i034p08087.

Chapman, J. F., and I. H. Cairns (2003), Three-dimensional modeling of Earth's bow shock: Shock shape as a function of Alfvén Mach number, *J. Geophys. Res.*, *108*, 1174–1184, doi:10.1029/2002JA009569.

Coroniti, F. V., and C. F. Kennel (1972), Changes in magnetospheric configuration during the substorm growth phase, *J. Geophys. Res.*, *77*, 3361–3370, doi:10.1029/JA077i019p03361.

DiBraccio, G. A., J. A. Slavin, S. A. Boardsen, B. J. Anderson, H. Korth, T. H. Zurbuchen, J. M. Raines, D. N. Baker, R. L. McNutt Jr., and S. C. Solomon (2013), MESSENGER observations of magnetopause structure and dynamics at Mercury, *J. Geophys. Res. Space Physics*, doi:10.1002/jgra50123, in press.

Fairfield, D. H. (1971), Average and unusual locations of the Earth's magnetopause and bow shock, *J. Geophys. Res.*, *76*, 6700–6716, doi:10.1029/JA076i028p06700.

Fairfield, D. H. (1995) Observations of the shape and location of the magnetopause: A review, in *Physics of the Magnetopause*, edited by P. Song, U. Bengt, Ö. Sonnerup, and M. F. Thomsen, pp. 53–60, *Geophys. Monogr. Ser.*, vol. 90, AGU, Washington, D. C.

Farris, M. H., and C. T. Russell (1994), Determining the standoff distance of the bow shock: Mach number dependence and use of models, *J. Geophys. Res.*, *99*, 17,681–17,689, doi:10.1029/94JA01020.

Formisano, V., P. C. Hedgecock, G. Moreno, J. Sear, and D. Bollea (1971), Observations of Earth's bow shock for low Mach numbers, *Planet. Space Sci.*, *19*, 1519–1531, doi:10.1016/0032-0633(71)90011-0.

Fuselier, S. A., B. J. Anderson, and T. G. Onsager (1995), Particle signatures of magnetic topology at the magnetopause: AMPTE/CCE observations, *J. Geophys. Res.*, *100*, 11,805–11,821, doi:10.1029/94JA02811.

Fuselier, S. A., B. J. Anderson, and T. G. Onsager (1997), Electron and ion signatures of field line topology at the low shear magnetopause, *J. Geophys. Res.*, *102*, 4847–4863, doi:10.1029/96JA03635.

Gershman, D. J., T. H. Zurbuchen, L. A. Fisk, J. A. Gilbert, J. M. Raines, B. J. Anderson, C. W. Smith, H. Korth, and S. C. Solomon (2012), Solar wind alpha particles and heavy ions in the inner heliosphere, *J. Geophys. Res.*, *117*, A00102, doi:10.1029/2012JA017829.

Glassmeier, K.-H., J. Grosser, U. Auster, D. Constantinescu, Y. Narita, and S. Stellmach (2007), Electromagnetic induction effects and dynamo action in the Hermean system, *Space Sci, Rev.*, *132*, 511–527, doi:10.1007/s11214-007-9244-9.

Goldstein, B. E., S. T. Seuss, and R. J. Walker (1981), Mercury: Magnetospheric processes and the atmospheric supply and loss rates, *J. Geophys. Res.*, *86*, 5485–5499, doi:10.1029/JA086iA07p05485.

Greenstadt, E. W. (1991), Quasi-perpendicular/quasi-parallel divisions of Earth's bow shock, *J. Geophys. Res.*, *96*, 1697–1703, doi:10.1029/90JA01759.

Grosser, J., K.-H. Glassmeier, and A. Stadelmann (2004), Induced magnetic field effects at planet Mercury, *Planet. Space Sci.*, *52*, 1251–1260, doi:10.1016/j.pss.2004.08.005.

Holzer, R. E., and J. A. Slavin (1978), Magnetic flux transfer associated with expansions and contractions of the dayside magnetosphere, *J. Geophys. Res.*, *83*, 3831–3839, doi:10.1029/JA083iA08p03831.

Johnson, C. L., et al. (2012), MESSENGER observations of Mercury's magnetic field structure, *J. Geophys. Res.*, *117*, E00L14, doi:10.1029/2012JE004217.

Joy, S. P., M. G. Kivelson, R. J. Walker, K. K. Khurana, C. T. Russell, and T. Ogino (2002), Probabilistic models of the Jovian magnetopause and bow shock locations, *J. Geophys. Res.*, *107*, 1309, doi:10.1029/2001JA009146.

Kabin, K., T. I. Gombosi, D. L. DeZeeuw, and K. G. Powell (2000), Interaction of Mercury with the solar wind, *Icarus*, *143*, 397–406, doi:10.1006/icar.1999.6252.

Korth, H., B. J. Anderson, T. H. Zurbuchen, J. A. Slavin, S. Perri, S. A. Boardsen, D. N. Baker, S. C. Solomon, and R. L. McNutt Jr. (2010), The interplanetary magnetic field at Mercury's orbit, *Planet. Space Sci.*, *59*, 2075–2085, doi:10.1016/j.pss.2010.10.014.

Lin, R. L., X. X. Zhang, S. Q. Liu, Y. L. Wang, and J. C. Gong (2010), A three-dimensional asymmetric magnetopause model, *J. Geophys. Res. 115*, A04207, doi:10.1029/2009JA014235.

Lu, J. Y., Z.-Q. Liu, K. Kabin, M. X. Zhao, D. D. Liu, Q. Zhou, and Y. Xiao (2011), Three dimensional shape of the magnetopause: Global MHD results, *J. Geophys. Res.*, *116*, A09237, doi:10.1029/2010JA016418.

Müller, J., S. Simon, Y.-C. Wang, U. Motschmann, D. Heyner, J. Schüle, W.-H. Ip, G. Kleindienst, and G. J. Pringle (2012), Origin of Mercury's double magnetopause: 3D hybrid simulation study with A.I.K.E.F, *Icarus*, *218*, 666–687, doi:10.1016/j.icarus.2011.12.028.

Odstrcil, D. (2003), Modeling 3-D solar wind structure, *Adv. Space Res.*, *32*, 497–506, doi:10.1016/S0273-1177(03)00332-6.

Peredo, M., J. A. Slavin, E. Mazur, and S. A. Curtis (1995), Three-dimensional position and shape of the bow shock and their variation with Alfvénic, sonic and magnetosonic Mach numbers and interplanetary magnetic field orientation, *J. Geophys. Res.*, *100*, 7907–7916, doi:10.1029/94JA02545.

Russell, C. T. (1977), On the relative locations of the bow shocks of the terrestrial planets, *Geophys. Res. Lett.*, *4*, 387–390, doi:10.1029/GL004i010p00387.

Russell, C. T., D. N. Baker, and J. A. Slavin (1988), The magnetosphere of Mercury, in *Mercury*, edited by F. Vilas, C. R. Chapman, and M. S. Matthews, pp. 514–561, University of Arizona Press, Tucson, Ariz.

Seuss, S. T., and B. E. Goldstein (1979), Compression of the hermean magnetosphere by the solar wind, *J. Geophys. Res.*, *84*, 3306–3312, doi:10.1029/JA084iA07p03306.

Shue, J.-H., J. K. Chao, H. C. Fu, C. T. Russell, P. Song, K. K. Khurana, and H. J. Singer (1997), A new functional form to study the solar wind control of the magnetopause size and shape, *J. Geophys. Res.*, *102*, 9497–9511, doi:10.1029/97JA00196.

Shue, J.-H., P. Song, C. T. Russell, J. K. Chao, and Y.-H. Yang (2000), Toward predicting the position of the magnetopause within geosynchronous orbit, *J. Geophys. Res.*, *105*, 2641–2656, doi:10.1029/1999JA900467.

Sibeck, D. G., R. E. Lopez, and E. C. Roelof (1991), Solar wind control of the magnetopause shape, location, and motion, *J. Geophys. Res.*, *96*, 5489–5495, doi:10.1029/90JA02464.

Slavin, J. A. (2004), Mercury's magnetosphere, *Adv. Space Res.*, *33*, 1859–1874, doi:10.1016/j.asr.2003.02.019.

Slavin, J. A., and R. E. Holzer (1979), The effect of erosion on the solar wind standoff distance at Mercury, *J. Geophys. Res.*, *84*, 2076–2082, doi:10.1029/JA084iA05p02076.

Slavin, J. A., and R. E. Holzer (1981), Solar wind flow about the terrestrial planets 1. Modeling bow shock position and shape, *J. Geophys. Res.*, *86*, 11,401–11,418, doi:10.1029/JA086iA13p11401.

Slavin, J. A., R. E. Holzer, J. R. Spreiter, S. S. Stahara, and D. S. Chaussee (1983a), Solar wind flow about the terrestrial planets, 2. Comparison with gas dynamic theory and implications for solar-planetary interactions, *J. Geophys. Res.*, *88*, 19–35, doi:10.1029/JA088iA01p00019.

Slavin, J. A., B. T. Tsurutani, E. J. Smith, D. E. Jones, and D. G. Sibeck (1983b), Average configuration of the distant (<220 R_e) magnetotail: Initial ISEE-3 magnetic field results, *Geophys. Res. Lett.*, *10*, 973–976, doi:10.1029/GL010i010p00973.

Slavin, J. A., R. E. Holzer, J. R. Spreiter, and S. S. Stahara (1984), Planetary Mach cones: Theory and observation, *J. Geophys. Res.*, *89*, 2708–2714, doi:10.1029/JA089iA05p02708.

Slavin, J. A., et al. (2009), MESSENGER observations of Mercury's magnetosphere during northward IMF, *Geophys. Res. Lett.*, *36*, L02101, doi:10.1029/2008GL036158.

Slavin, J. A., et al. (2010), MESSENGER observations of extreme loading and unloading of Mercury's magnetic tail, *Science*, *329*, 665–668, doi:10.1126/science.1188067.

Slavin, J. A., et al. (2012a), MESSENGER and Mariner 10 flyby observations of magnetotail structure and dynamics at Mercury, *J. Geophys. Res.*, *117*, A01215, doi:10.1029/2011JA016900.

Slavin, J. A., et al. (2012b), MESSENGER observations of a flux-transfer-event shower at Mercury, *J. Geophys. Res.*, *117*, A00M06, doi:10.1029/2012JA017926.

Spreiter, J. R., and S. S. Stahara (1980), A new predictive model for determining solar wind–terrestrial planet interactions, *J. Geophys. Res.*, *85*, 6769–6777, doi:10.1029/JA085iA12p06769.

Spreiter, J. R., and S. S. Stahara (1985), Magnetohydrodynamic and gasdynamic theories for planetary bow waves, in *Collisionless Shocks in the Heliosphere: A Review of Current Research*, edited by B. Tsurutani and T. R. G. Stone, pp. 85–107, *Geophys. Monogr. Ser.*, vol. 35, AGU, Washington, D. C.

Spreiter, J. R., A. L. Summers, and A. Y. Alksne (1966), Hydromagnetic flow around the magnetosphere, *Planet. Space Sci.*, *14*, 223–250, doi:10.1016/0032-0633(66)90124-3.

Sundberg, T., S. A. Boardsen, J. A. Slavin, B. J. Anderson, H. Korth, T. H. Zurbuchen, J. M. Raines, and S. C. Solomon (2012), MESSENGER orbital observations of large-amplitude Kelvin-Helmholtz waves at Mercury's magnetopause, *J. Geophys. Res.*, *117*, A04216, doi:10.1029/2011JA017268, 2012.

Verigin, M., J. Slavin, A. Szabo, T. Gombosi, G. Kotova, O. Plochova, K. Szegö, M. Tátrallyay, K. Kabin, and F. Shugaev (2003a), Planetary bow shocks: Gasdynamic analytic approach, *J. Geophys. Res.*, *108*, 1323, doi:10.1029/2002JA009711.

Verigin, M., J. Slavin, A. Szabo, G. Kotova, and T. Gombosi (2003b), Planetary bow shocks: Asymptotic MHD Mach cones, *Earth Planets Space*, *55*, 33–38.

Winslow, R. M., C. L. Johnson, B. J. Anderson, H. Korth, J. A. Slavin, M. E. Purucker, and S. C. Solomon (2012), Observations of Mercury's northern cusp region with MESSENGER's Magnetometer, *Geophys. Res. Lett.*, *39*, L08112, doi:10.1029/2012GL051472.

Zwickl, R. D., D. N. Baker, S. J. Bame, W. C. Feldman, J. T. Gosling, E. W. Jr.Hones, D. J. McComas, B. T. Tsurutani, and J. A. Slavin (1984), Evolution of the Earth's distant magnetotail: ISEE 3 electron plasma results, *J. Geophys. Res.*, *89*, 11,007–11,012, doi:10.1029/JA089iA12p11007.